The Astrophysical Journal, 948:105 (13pp), 2023 May 10 https://doi.org/10.3847/1538-4357/acbf51

The Locations of Features in the Mass Distribution of Merging Binary Black Holes Are Robust against Uncertainties in the Metallicity-dependent Cosmic Star Formation History

L. A. C. van Son[1,2,3], S. E. de Mink[2,3], M. Chruślińska[3], C. Conroy[1], R. Pakmor[3], and L. Hernquist[1]
[1] Center for Astrophysics, Harvard & Smithsonian, 60 Garden St., Cambridge, MA 02138, USA; lieke.van.son@cfa.harvard.edu
[2] Anton Pannekoek Institute of Astronomy, Science Park 904, University of Amsterdam, 1098XH Amsterdam, The Netherlands
[3] Max Planck Institute for Astrophysics, Karl-Schwarzschild-Str. 1, D-85748 Garching, Germany
Received 2022 September 6; revised 2023 February 24; accepted 2023 February 24; published 2023 May 11

Abstract

New observational facilities are probing astrophysical transients such as stellar explosions and gravitational-wave sources at ever-increasing redshifts, while also revealing new features in source property distributions. To interpret these observations, we need to compare them to predictions from stellar population models. Such models require the metallicity-dependent cosmic star formation history ($\mathcal{S}(Z, z)$) as an input. Large uncertainties remain in the shape and evolution of this function. In this work, we propose a simple analytical function for $\mathcal{S}(Z, z)$. Variations of this function can be easily interpreted because the parameters link to its shape in an intuitive way. We fit our analytical function to the star-forming gas of the cosmological TNG100 simulation and find that it is able to capture the main behavior well. As an example application, we investigate the effect of systematic variations in the $\mathcal{S}(Z, z)$ parameters on the predicted mass distribution of locally merging binary black holes. Our main findings are that (i) the locations of features are remarkably robust against variations in the metallicity-dependent cosmic star formation history, and (ii) the low-mass end is least affected by these variations. This is promising as it increases our chances of constraining the physics that govern the formation of these objects (https://github.com/LiekeVanSon/SFRD_fit/tree/7348a1ad0d2ed6b78c70d5100fb3cd2515493f02/).

Unified Astronomy Thesaurus concepts: Star formation (1569); Gravitational wave astronomy (675); Astrophysical black holes (98); Stellar mass black holes (1611)

1. Introduction

A myriad of astrophysical phenomena depends critically on the rate of star formation throughout the cosmic history of the universe. Exotic transient phenomena, including (pulsational) pair-instability supernovae, long gamma-ray bursts, and gravitational-wave (GW) events appear to be especially sensitive to the metallicity at which star formation occurs at different epochs throughout the universe (e.g., Fruchter et al. 2006; Langer et al. 2007; Abbott et al. 2016). Gravitational astronomy in particular has seen explosive growth in the number of detections in the past decade (Abbott et al. 2019, 2021a, 2021b), while theoretical predictions vary greatly due to uncertainties in the aforementioned metallicity of star formation (e.g., Broekgaarden et al. 2022; Santoliquido et al. 2021). In order to correctly model and interpret these observations, it is thus fundamental to know the rate of star formation at different metallicities throughout cosmic history, i.e., the metallicity-dependent cosmic star formation history ($\mathcal{S}(Z, z)$, see also the recent review by Chruślińska 2022). Throughout this work, little z refers to the redshift and Z to the metallicity of star formation.

It is difficult to observationally constrain the shape of $\mathcal{S}(Z, z)$ (see, e.g., Chruślińska & Nelemans 2019; Boco et al. 2021, for discussion of relevant observational caveats). Even at low redshifts, the low-metallicity part of the distribution is poorly constrained (Chruślińska et al. 2021). Nonetheless, several methods exist to estimate the metallicity-dependent cosmic star formation history.

The first method is based on empirical scaling relations, linking galaxy properties like stellar mass $M_\star$, metallicity Z, and overall star formation rate density, SFRD(z), with the galaxy stellar mass function (GSMF; see, e.g., Dominik et al. 2013). However, the applied methods to infer galaxy properties and subsequently scaling relations such as the MZ relation differ greatly, which makes it difficult to interpret these results in a consistent way (e.g., Kewley & Ellison 2008; Cresci et al. 2019; Maiolino & Mannucci 2019). Moreover, observations are generally incomplete at high redshifts and low galaxy luminosity (e.g., Chruślińska et al. 2021).

One can also directly extract the metallicity-dependent cosmic star formation history from cosmological simulations (e.g., Mapelli et al. 2017; Briel et al. 2022). However, these simulations currently lack the resolution to resolve the lowest mass galaxies, and their variations in $\mathcal{S}(Z, z)$ span a smaller range than those observed in observationally based models (Pakmor et al. 2022).

Alternatively, one can combine analytical models for the observed overall SFRD(z), like those from Madau & Dickinson (2014) or Madau & Fragos (2017), and convolve this with an assumed function for the shape of the cosmic metallicity density distribution, such as was done in, e.g., Langer & Norman (2006) and the phenomenological model in Neijssel et al. (2019).

In this work, we follow the latter approach and propose a flexible analytical model for $\mathcal{S}(Z, z)$ that can be fit to the output of both cosmological simulations, and observational data constraints where available. In contrast to earlier work, we adopt a skewed-log normal distribution of metallicities that can capture the asymmetry in the low and high-metallicity tails.

The purpose of this proposed form is twofold. First of all, the form we propose allows for an intuitive interpretation of the free parameters. This allows us to obtain better insight into the impact of changes in these parameters on the inferred ranges of astrophysical transients (as we demonstrate in Section 4 using GW predictions as an example). By adopting an analytical, parametrized form for $\mathcal{S}(Z, z)$, the large uncertainties can be systematically explored. Second, both the large complications in observational constraints, and the many uncertainties in cosmological simulations call for a generalized form of $\mathcal{S}(Z, z)$ that can be easily updated when new information becomes available. In particular, the advent of observations with JWST promises a new era of high-redshift metallicity studies of previously unexplored regimes (e.g., Sanders et al. 2023). We hope that this form will facilitate the flexibility needed to keep up with observations. The model described in this work is incorporated in the publicly available Cosmic Integration suite of the `COMPAS` code.[4]

We describe our model for $\mathcal{S}(Z, z)$ in Section 2. We fit our model to the star-forming gas in the Illustris TNG100 simulation in Section 3, and demonstrate an example application of our model by systematically varying the parameters that determine the shape of $\mathcal{S}(Z, z)$ and investigate their impact on the local distribution of merging binary black hole (BBH) masses in Section 4. We summarize our findings in Section 5.

Throughout this work, we adopt a universal Kroupa initial mass function (Kroupa 2001) with the mass limits 0.01–200 $M_\odot$ and a flat ΛCDM cosmology with $\Omega_M = 0.31$, $\Omega_\Lambda = 0.69$, and $H_0 = 67.7\ \mathrm{km\,s^{-1}\,Mpc^{-1}}$ (Planck Collaboration et al. 2020).

2. A Convenient Analytic Expression for the Metallicity-dependent Cosmic Star Formation History

We write the metallicity-dependent cosmic star formation history as

$$\boxed{\mathcal{S}(Z, z) = \mathrm{SFRD}(z) \times \frac{dP}{dZ}(Z, z)} \tag{1}$$

(similar to, e.g., Langer & Norman 2006). The first term is the SFRD(z), which is the amount of mass formed in stars per unit of time and per unit of comoving volume at each redshift, z. The second term, $dP/dZ(Z, z)$, is a probability density distribution that expresses what fraction of star formation occurs at which metallicity, Z, at each redshift.

2.1. The Cosmic Metallicity Density Distribution

For the probability distribution of metallicities, we draw inspiration from the approach by, e.g., Neijssel et al. (2019) who used a log-normal distribution for their phenomenological model. Unfortunately, a simple log-normal distribution cannot capture the asymmetry that we see in the cosmological simulations, which show an extended tail in $\log_{10} Z$ toward low metallicity, combined with a very limited tail toward higher metallicity. To capture this behavior we adopt a skewed log-normal distribution instead. This is an extension of the normal distribution that introduces an additional shape parameter, α, that regulates the skewness (first introduced by O'Hagan & Leonard 1976).

The skewed log-normal distribution of metallicities is defined as

$$\begin{aligned}\frac{dP}{dZ}(Z, z) &= \frac{1}{Z} \times \frac{d(Z, z)}{d\ln Z}\\ &= \frac{1}{Z} \times \frac{2}{\omega}\underbrace{\phi\left(\frac{\ln Z - \xi}{\omega}\right)}_{(a)}\underbrace{\Phi\left(\alpha\frac{\ln Z - \xi}{\omega}\right)}_{(b)},\end{aligned} \tag{2}$$

where (a) is the standard log-normal distribution, ϕ,

$$\phi\left(\frac{\ln Z - \xi}{\omega}\right) \equiv \frac{1}{\sqrt{2\pi}}\exp\left\{-\frac{1}{2}\left(\frac{\ln Z - \xi}{\omega}\right)^2\right\}, \tag{3}$$

and (b) is the new term that allows for asymmetry, which is equal to the cumulative of the log-normal distribution, Φ,

$$\Phi\left(\alpha\frac{\ln Z - \xi}{\omega}\right) \equiv \frac{1}{2}\left[1 + \mathrm{erf}\left\{\alpha\frac{\ln Z - \xi}{\omega\sqrt{2}}\right\}\right]. \tag{4}$$

This introduces three parameters, α, ω, and ξ, each of which may depend on redshift. The first parameter, α, is known as the *shape*. It affects the skewness of the distribution and thus allows for asymmetries between metallicities that are higher and lower than the mean. The symmetric log-normal distribution is recovered for $\alpha = 0$. The second parameter, ω is known as the *scale*. It provides a measure of the spread in metallicities at each redshift. Finally, ξ, is known as the *location* because this parameter plays a role in setting the mean of the distribution at each redshift.

The location and the mean of the metallicity distribution: To obtain a useful expression for the redshift dependence of the location $\xi(z)$ we first express the expected value or mean metallicity at a given redshift

$$\langle Z\rangle = 2\exp\left(\xi + \frac{\omega^2}{2}\right)\Phi(\beta\,\omega), \tag{5}$$

where β is

$$\beta = \frac{\alpha}{\sqrt{1 + \alpha^2}}. \tag{6}$$

(For a more extended derivation of the moments of the skewed log normal, see, e.g., Wang et al. 2019.)

For the evolution of the mean metallicity with redshift we follow Langer & Norman (2006) and the phenomenological model from Neijssel et al. (2019) in assuming that the mean of the probability density function of metallicities evolves with redshift as

$$\langle Z\rangle \equiv \mu(z) = \mu_0 \cdot 10^{\mu_z \cdot z}, \tag{7}$$

where μ_0 is the mean metallicity at redshift 0, and μ_z determines the redshift evolution of the location. Equating this to Equation (5), we get an expression for $\xi(z)$,

$$\xi(z) = \ln\left(\frac{\mu_0 \cdot 10^{\mu_z \cdot z}}{2\,\Phi(\beta\,\omega)}\right) - \frac{\omega^2}{2}. \tag{8}$$

The scale (and variance) of the metallicity distribution: We will also allow the scale ω to evolve with redshift in a similar

---

[4] https://github.com/TeamCOMPAS/COMPAS/tree/dev/utils/CosmicIntegration

manner,

$$\omega(z) = \omega_0 \cdot 10^{\omega_z \cdot z}, \tag{9}$$

where ω_0 is the width of the metallicity distribution at $z = 0$, and ω_z the redshift evolution of the scale.

Note that the width, $w(z)$ is not the same as the variance. The variance, $\sigma^2(z)$, can be expressed as

$$\sigma^2(z) = \omega^2(z)\left(1 - \frac{2\beta^2}{\pi}\right). \tag{10}$$

Asymmetry of the metallicity distribution—α: The skewness α could in principle also be allowed to evolve with redshift (e.g., $\alpha(z) = \alpha(z = 0)10^{\alpha_z \cdot z}$). However, we find no significant improvement over the simpler assumption where alpha is kept constant. Note that the redshift evolution of the scale (Equation (9)), already captures similar behavior in our current formalism. We therefore adopt $\alpha = \alpha(z = 0)$ and $\alpha_z = 0$.

In summary, Equation (2) becomes

$$\boxed{\frac{dP}{dZ}(Z, z) = \frac{2}{\omega(z)Z} \times \phi\left(\frac{\ln Z - \xi(z)}{\omega(z)}\right)\Phi\left(\alpha\frac{\ln Z - \xi(z)}{\omega(z)}\right)}, \tag{11}$$

where $\xi(z)$ and $\omega(z)$ are defined in Equations (8) and (9), respectively, and we have assumed α to be constant.

2.2. The Overall Cosmic Star Formation Rate Density

For the SFRD, we assume the analytical form proposed by Madau & Dickinson (2014),

$$\boxed{\mathrm{SFRD}(z) = \frac{d^2M_{\mathrm{SFR}}}{dtdV_c}(z) = a\frac{(1+z)^b}{1 + [(1+z)/c]^d}} \tag{12}$$

in units of $[M_\odot\ \mathrm{yr}^{-1}\ \mathrm{cMpc}^{-3}]$. This introduces four parameters: a which sets the overall normalization and which has the same units as SFRD(z) and b, c, and d, which are unitless and which govern the shape of the overall cosmic SFR with redshift.

Lastly, we combine Equations (11) and (12) to form a full metallicity-specific SFR as described in Equation (1).

3. Fit against Cosmological Simulation

We fit our new functional form of $\mathcal{S}(Z, z)$ as defined by Equations (1), (11), and (12) to the IllustrisTNG cosmological simulations. We simultaneously fit for the following nine free parameters α, μ_0, μ_z, ω_0, and ω_z, which govern the metallicity dependence and a–d, which set the overall SFRD(z). Below we briefly discuss the IllustrisTNG simulations and elaborate on our fitting procedure.

3.1. IllustrisTNG Cosmological Simulations

Although here, we only fit our model to the TNG100 simulation, our prescription can be easily used to fit other simulated or observational data of the metallicity-dependent cosmic star formation history.[5]

The IllustrisTNG-project (or TNG in short) considers galaxy formation and evolution through large-scale cosmological hydrodynamical simulations (Marinacci et al. 2018; Naiman et al. 2018; Nelson et al. 2018, 2019a; Pillepich et al. 2018a, 2019; Springel et al. 2018). Such simulations provide the tools to study parts of the universe that are not easily accessible by observations. In particular of interest for this work, they simulate the high-redshift enrichment of galaxies and the tail of low-metallicity star formation at low redshift.

The models implemented in the publicly available TNG simulations (Nelson et al. 2019b)[6] have led to many successes. These models were calibrated at the resolution of the TNG100 simulation; hence, TNG100 is expected to provide the best overall agreement to global properties (like the SFR). This is why we adopt the TNG100 simulation as our fiducial simulation. For a more extended discussion focused on the processes that govern the creation, distribution, and mixing of metals in the TNG simulations, we refer to Pakmor et al. (2022). In short, star formation in the TNG simulations is calibrated against the Kennicutt–Schmidt relation (Schmidt 1959; Kennicutt 1989), using an effective equation of state (Springel & Hernquist 2003). The stellar metallicity yields are an updated version of the original Illustris simulations as described in Pillepich et al. (2018b). Star particles deposit metals into the gas through type Ia and type II supernovae, as well as through asymptotic giant branch stars. The TNG simulations have been shown to match observational constraints on the mass–metallicity relation of galaxies up to $z = 2$ (Torrey et al. 2019), as well as iron abundances (Naiman et al. 2018), metallicity gradients within galaxies at low redshift (Hemler et al. 2021), and the reduction of star formation in the centers of star-forming galaxies (Nelson et al. 2021). Several studies have used the TNG simulations to make predictions for astronomical transient sources (e.g., Bavera et al. 2022; Briel et al. 2022; van Son et al. 2022a). Out of the four $\mathcal{S}(Z, z)$ variations explored, Briel et al. (2022) find that TNG provides one of the best agreements between observed and predicted cosmic rates for electromagnetic and GW transients, when combined with their fiducial binary population synthesis model.

On the other hand, large uncertainties and crude approximations remain in all contemporary cosmological simulations, thus also in the TNG simulations. Generally, some of the chemical evolution of galaxies in cosmological simulations is unresolved, and thus depends strongly on the implemented *subgrid physics*. A known uncertainty is that dust is not included in the TNG simulations, which could mean that metallicity of the star-forming gas is overestimated. Feedback from active galactic nuclei is not well understood theoretically and is described in an approximate manner (Springel et al. 2005; Weinberger et al. 2017). Furthermore, all stellar winds' mass loss from massive stars, binary interactions, and their ionizing effects are ignored (e.g., Dray et al. 2003; Smith 2014; Götberg et al. 2020; Doughty & Finlator 2021; Farmer et al. 2021; Goswami et al. 2022). Moreover, the uniform ionizing UV background is turned on abruptly at $z = 6$. This crucially impacts the amount of low-metallicity star formation at high redshift as it allows small galaxies to produce more stars than what would be expected for a gradually increasing UV background that reaches full strength at $z = 6$. All these uncertainties underline the need for a flexible approximation of the $\mathcal{S}(Z, z)$ that can be easily updated when cosmological models and sub-grid physics are updated.

---

[5] We provide a Jupyter notebook to facilitate this fit here: https://github.com/LiekeVanSon/SFRD_fit/blob/main/src/scripts/Notebooks/Fit_model_to_sfrdzZ.ipynb.

[6] https://www.tng-project.org/

Table 1
Best-fitting Parameters for Our $\mathcal{S}(Z, z)$ Fit to TNG100 Data

dP/dZ	Description	Best Fit	SFRD(z) ($M_\odot$ yr^{-1} Mpc^{-3})	Best Fit
μ_0	Mean metallicity at $z = 0$	0.025 ± 0.036	a	0.02 ± 0.072
μ_z	z-dependence of the mean	-0.049 ± 0.006	b	1.48 ± 0.002
α	Shape (skewness)	-1.778 ± 0.002	c	4.44 ± 0.001
ω_0	Scale at $z = 0$	1.122 ± 0.001	d	5.90 ± 0.002
ω_z	z-dependence of the scale	0.049 ± 0.009		

3.2. Choices and Binning of the Data

We fit Equation (1) to the metallicity-dependent star formation rate (SFR) of the star-forming gas in the TNG100 simulation. For this, we use a binned version of the TNG data $\mathcal{S}(Z, z)_{\rm sim}$. We consider metallicities between $\log_{10} Z = -5$ and $\log_{10} Z = 0$ in 30 bins, where we use Z_i to refer to the logarithmic centers of the bins. We ignore star formation in metallicities $\log_{10} Z \leqslant -5$ as this accounts for less than 1% of the total cosmic SFR in these simulations. We consider bins in redshifts between $z = 0$ and $z = 10$, with a step size of $dz = 0.05$, where z_j refers to the centers of the bins.

3.3. Optimization Function

To find a solution we use a method based on the sum of the quadratic differences between the simulations and our fit function. Using a vanilla χ-squared approach does not serve our purposes very well as it does a poor job in fitting regions where the star formation is very low. Using a χ-squared approach on the logarithm of the function instead places far too much weight on trying to fit the SFR in regions where the rate is very low or not even significant. After experimenting, we find that the following approach gives us satisfactory results.

We first consider a given redshift z_j. For this redshift, we compute the sum of the squared residuals between the cosmological simulation and our fit. This is effectively the square of the l^2 norm:

$$\chi^2(z_j) \equiv \sum_{Z_i} (\mathcal{S}(Z_i, z_j)_{\rm sim} - \mathcal{S}(Z_i, z_j)_{\rm fit})^2. \tag{13}$$

Here, the variable Z_i runs over all metallicity bins. We are particularly interested in properly fitting the low-metallicity star formation at high redshifts. At high redshifts, the overall SFRD(z) is generally lower. To ensure that our fitting procedure gives sufficient weight to the behavior at all redshifts, we introduce a penalization factor to somewhat reduce the contribution of redshifts where the peak of cosmic star formation occurs, while increasing the weight at redshifts where the overall SFRD(z) is lower. To achieve this we divide $\chi^2(z_j)$ by the star formation $\sum_{Z_i} \mathcal{S}(Z_i, z_j)$ per redshift bin before adding the contribution of all redshifts. Our final expression for the cost function reads as

$$\chi = \sum_{z_j} \frac{\chi^2(z_j)}{\sum_{Z_i} \mathcal{S}(Z_i, z_j)}. \tag{14}$$

To minimize this cost function, we use `scipy.optimize.minimize` from SciPy v1.6.3, which implements the quasi-Newton method of Broyden, Fletcher, Goldfarb, and Shanno (Nocedal & Wright 2006).

3.4. Resulting $\mathcal{S}(Z, z)$

Our best-fitting parameters are listed in Table 1. With these fit parameters, $\chi^2(z_j)$ is smaller than 2×10^{-4} at any given redshift. To evaluate our fit, we show the absolute residuals and relative errors in Appendix A. We will refer to the $\mathcal{S}(Z, z)$ with the parameters listed in Table 1 as our fiducial model.

In Figure 1 we show our fiducial model at different redshifts and metallicities. We also show the overall SFRD(z) in Figure 2. In general, our analytical model captures the metallicity-dependent cosmic star formation history in the TNG100 simulations well (bottom panels of Figure 1). The skewed log-normal metallicity distribution is able to reproduce the overall behavior that is observed in TNG100 (bottom left panel, but see Pakmor et al. 2022, for an in-depth discussion of low-metallicity star formation in the TNG50 simulation). Only minor features like the additional bump just above $\log_{10}(Z) = -2$ at redshift 2 are missed. However, for our purposes, it is more important to prioritize fitting the large-scale trends, while we are not so interested in smaller scale fluctuations.

Adopting a skewed-log normal metallicity distribution allows for a tail of low-metallicity star formation out to low redshifts. To emphasize the difference between a skewed-log normal and a symmetric log-normal distribution, we show the phenomenological model from Neijssel et al. (2019) in dotted gray. Their model falls within the family of functions that is encompassed by our model described in Section 2, but we note that their model is distinctly different.[7]

Although our model performs well at reproducing the large-scale trends seen in TNG, we acknowledge that more complex features as suggested by some observational studies could be missed. One example is that the SFRD(z) shape we adopt from Madau & Dickinson (2014) does not account for starburst galaxies (see the discussion in Chruślińska et al. 2021). Moreover, our model cannot capture inflection points in the mean metallicity because we assume both μ_0 and μ_z are constants with redshift (Equation (7)). Contrarily, Chruślińska & Nelemans (2019) find an upturn in the amount of low-metallicity star formation above $z = 4$ if the power law of the GSMF is allowed to evolve with redshift. Hence, although our model is more broadly applicable than previous models, in it is current form, it does not capture the complete range of observationally allowed variations. Incorporating more complex functional forms for our model, the mean metallicity could possibly capture such behavior, but this analysis is beyond the scope of this paper.

---

[7] The phenomenological model from Neijssel et al. (2019) is recovered by adopting $\mu_0 = 0.035$, $\mu_z = -0.23$, $\omega_0 = 0.39$, $\omega_z = 0$, $\alpha = 0$, $a = 0.01$, $b = 2.77$, $c = 2.9$, and $d = 4.7$.

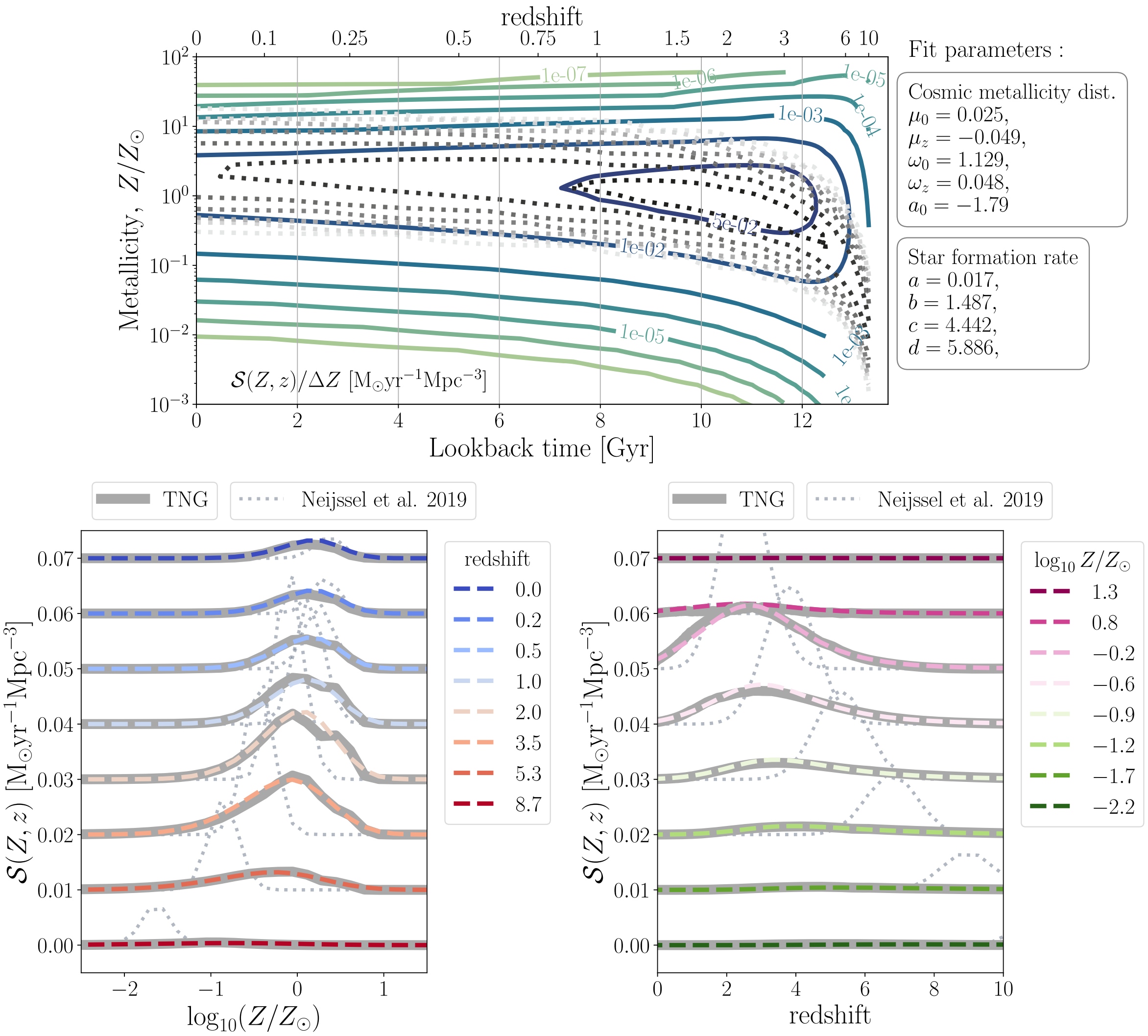

Figure 1. Our fiducial $\mathcal{S}(Z, z)$ model, adopting the best-fitting parameters (listed on the top right) to fit the TNG100 simulations. The top panel shows the full two-dimensional $\mathcal{S}(Z, z)$ linear in time. Contours range from 10^{-7}–$10^{-2} M_\odot$ yr^{-1} Mpc^{-3}. The bottom left (right) panel shows slices of the distribution in redshift (metallicity). Each slice is displaced by $0.01 M_\odot$ yr^{-1} Mpc^{-3} (note the linear scale of $\mathcal{S}(Z, z)$ in the bottom panel). We show the TNG100 simulation data with thick gray lines. For comparison, we also show the phenomenological model from Neijssel et al. (2019) in all panels with gray dotted lines. The bottom panels show that our analytical model adequately captures the shape of the $\mathcal{S}(Z, z)$ from TNG100.

4. Application: Systematic Variations of $\mathcal{S}(Z, z)$ and the Effect on the Mass Distribution of Merging BBHs

We will now demonstrate the application of our analytical model by systematically varying the parameters in our fiducial $\mathcal{S}(Z, z)$ model, and investigate their effect on the local mass distribution of BBH mergers originating from isolated binaries.

We use the publicly available rapid binary population synthesis simulations presented in van Son et al. (2022b) and available for download at doi:10.5281/zenodo.7612755. These simulations were run using version v02.26.03 of the open-source `COMPAS` suite (Riley et al. 2022).[8] `COMPAS` is based on algorithms that model the evolution of massive binary stars following Hurley et al. (2000, 2002) using detailed evolutionary models by Pols et al. (1998). In particular, we use the simulations behind Figure 1 from van Son et al. (2022b), and we refer the reader to their methods section for a detailed description of the adopted physics parameters and assumptions.[9] Metallicities of each binary system were sampled from a smooth probability distribution to avoid artificial peaks in the BH mass distribution (e.g., Dominik et al. 2015; Kummer 2020). These simulations provide us with an estimate of the yield of BBH mergers per unit of star-forming mass and metallicity.

We combine the aforementioned yield with variations of the fiducial $\mathcal{S}(Z, z)$ model described in this work. By integrating over cosmic history, we obtain the local merger rates of BBH systems, which allow us to construct the distribution of source properties at every redshift. We use the cosmic integration scheme that is part of the publicly available `COMPAS` suite, which includes the $\mathcal{S}(Z, z)$ model described in this work. The details of this framework are described in Neijssel et al. (2019),

---

[8] https://github.com/TeamCOMPAS/COMPAS

[9] We note that the rate in van Son et al. (2022b) is slightly higher than the fiducial rate presented in Figure 3 in this work. This difference is caused by the use of rounded parameter values of $\mathcal{S}(Z, z)$ in van Son et al. (2022b).

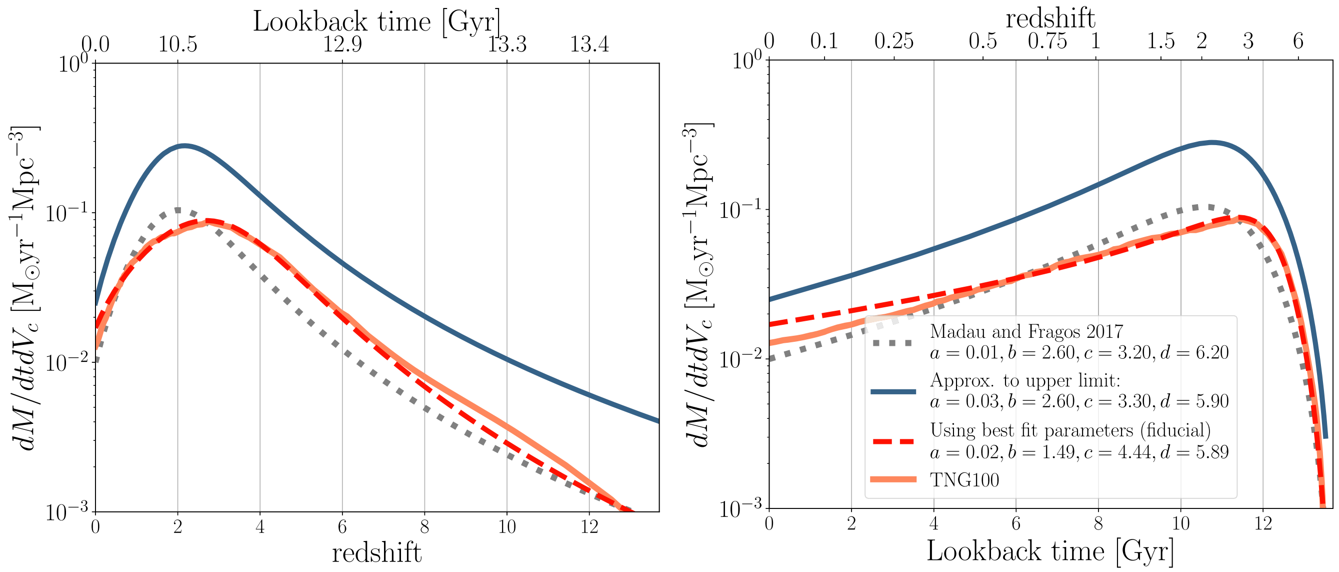

Figure 2. Comparison of several overall SFRD(z), with redshift (left panel) and with lookback time (right panel). The solid orange and dashed red lines, respectively, show the star formation data from TNG100 and our corresponding fit adopting Equation (12) (fiducial model). The dotted gray and solid blue lines are variations of Equation (12) used to approximate the lower and upper edge of possible star formation histories. The dotted gray line shows the model from Madau & Fragos (2017), while the solid blue line mimics the behavior of the power-law-fit to the `SB: B18/C17` variations with a nonevolving low-mass end of the GSFM from Chruślińska et al. (2021).

but also in van Son et al. (2022a), where more similar settings to this work are used.

4.1. Determining Reasonable Variations of $\mathcal{S}(Z, z)$

We consider variations in both the shape of the cosmic metallicity density distribution $dP/dZ(Z, z)$, and the shape of the overall SFR, SFRD(z). To determine the range that is reasonably allowed by observations, we compare our variations to the observation-based $\mathcal{S}(Z, z)$ models described in Chruślińska et al. (2021). An overview of the explored variations is shown in Table 2. Below we explain how we arrive at these values.

For the cosmic metallicity density distribution, we vary every parameter that determines the shape of $dP/dZ(Z, z)$ independently (three left-most columns of Table 1, and top of Table 2), while keeping all other parameters fixed at their fiducial value. For each variation, we inspect the fraction of stellar mass that is formed at low metallicity ($Z < 0.1 Z_\odot$) versus the fraction of stellar mass that is formed at high metallicity ($Z > Z_\odot$), for all star formation that occurred below a certain threshold redshift. We compare this to the models from Chruślińska et al. (2021) in Figure 6 in Appendix B. We have chosen our variations such that they span a reasonable range of cosmic metallicity density distributions as allowed by observation-based and cosmological simulations-based models. We use the models `214-f14SB-BiC_FMR270_FOH_z_dM.dat`, and `302-f14SB-Boco_FMR270_FOH_z_dM.dat` from Chruślińska et al. (2021)[10] as a representation of a very low and high-metallicity star formation realization respectively. These models are the low and high-metallicity extreme under their fiducial SFR–metallicity correlation, and so we will refer to them as `Chr21_lowZ` and `Chr21_highZ` respectively from hereon. The difference between these models lies in the assumptions in the underlying empirical galaxy relations. In general, low-mass galaxies contribute to low-metallicity star formation and shift the peak of $\mathcal{S}(Z, z)$ to lower metallicities. `Chr21_lowZ` is characterized by a star formation–galaxy mass relation that is flat at high galaxy masses (reducing the SFR for the highest-mass galaxies), a GSFM that evolves with redshift (predicting an increasing number density of low-mass galaxies), and a local galaxy mass–metallicity relation as in Pettini & Pagel (2004). This model further approximates the contribution of starburst galaxies following Bisigello et al. (2018) and Caputi et al. (2017). Assuming that starburst galaxies follow the empirical fundamental metallicity relation (leading to anticorrelation between the SFR and metallicity), their inclusion tends to shift the peak of $\mathcal{S}(Z, z)$ to lower metallicities and broadens the low-metallicity part of the distribution.

On the other hand, `Chr21_highZ` assumes the star formation–galaxy mass relation does not flatten toward higher galaxy masses, a GSFM where the slope for the low-mass end

Table 2
Variations on $\mathcal{S}(Z, z)$

	Min.	Fiducial	Max.
$dP/dZ(Z, z)$			
μ_0	0.007	0.025	0.035
μ_z	0.0	−0.049	−0.5
α	−6.0	−1.778	0.0
ω_0	0.7	1.125	2.0
ω_z	0.0	0.048	0.1
SFRD(z)			
(a, b ⋯	(0.01, 2.60	(0.02, 1.48	(0.03, 2.6
⋯ c, d)	3.20, 6.20)	4.44, 5.90)	3.3, 5.9)

Note. For every variation, we either swap the value of an individual $dP/dZ(Z, z)$ parameter, or exchange the set of four SFRD(z) parameters, and replace them by the min/max values listed here. All other parameters are kept fixed at their fiducial value.

---

[10] These models including a detailed description of their contents are publicly available at https://ftp.science.ru.nl/astro/mchruslinska/Chruslinska_et_al_2021/.

is constant over redshift, and a local galaxy mass–metallicity relation following Kobulnicky & Kewley (2004). Lastly, this model adopts the starburst prescription from Boco et al. (2021), which produces results that are similar to models without starburst galaxies.

For every variation of our model, we inspect both the full $\mathcal{S}(Z, z)$ and slices at redshifts $z = 0$, 0.5, 3.0, and 6 by eye. At each slice, we compare our model variation to `Chr21_lowZ` and `Chr21_highZ`, and ensure that none of our variations significantly exceeds these extremes in $\mathcal{S}(Z, z)$. This also serves as a sanity check for the overall SFR.

We also consider two variations of the overall SFRD(z), where we keep the metallicity distribution $dP/dZ(Z, z)$ fixed, but vary all four SFRD(z) parameters at once (right two columns of Table 1, and the bottom of Table 2). We use Figure 11 from Chruślińska et al. (2021) to determine approximate upper and lower bounds to the overall SFR. We choose Madau & Fragos (2017) as an approximation of the lower limit. For the upper limit, we use the upper edge of models that adopt starbursts following Bisigello et al. (2018) and Caputi et al. (2017) (`SB: B18/C17`), combined with a nonevolving low-mass end of the GSFM (shown as a thick brown line in Figure 11 of Chruślińska et al. 2021, and described in their Table B1). To approximate these models, we fit Equation (12) by eye to the broken power-law description of this model as presented in Appendix B1 of Chruślińska et al. (2021). We show all SFRD (z) variations in Figure 2.

4.2. Effect of the $\mathcal{S}(Z, z)$ on the Primary Masses of Merging BBH

To isolate the effect of the $\mathcal{S}(Z, z)$ from the effects of different formation channels, we split the data from van Son et al. (2022a) between the stable mass transfer channel (e.g., Inayoshi et al. 2017; van den Heuvel et al. 2017; Bavera et al. 2021; Gallegos-Garcia et al. 2021; Marchant et al. 2021; van Son et al. 2022a), and the *classical* common-envelope channel (or CE channel, e.g., Belczynski et al. 2007, 2016; Postnov & Yungelson 2014; Vigna-Gómez et al. 2018). These channels are distinguished based on whether the binary system has experienced a common envelope phase (CE channel) or only stable mass transfer (stable channel in short from now on).

In Figures 3 and 4, we show the resulting primary mass distribution of merging BBHs from the stable channel and CE channel, respectively. The primary (secondary) component refers to the more (less) massive component of merging BBHs. Each panel varies one aspect of the $\mathcal{S}(Z, z)$. In the first five panels of Figures 3 and 4, we vary one of the parameters that determine the shape of the probability density distribution of metallicities, while keeping all other values fixed at their fiducial values. In the last panel of Figures 3 and 4, we vary the shape of the overall SFRD(z) to one of the variations shown in Figure 2, while keeping the probability density distribution of metallicities fixed.

The first thing we note is that the locations of the features in the primary mass distribution are robust against variations in $\mathcal{S}(Z, z)$. For the stable channel, two features are visible in all variations: a peak at $M_{\rm BH,1} \approx 9 M_{\odot}$ and a bump at $M_{\rm BH,1} \approx 22 M_{\odot}$. Two more features are visible at the high mass end for almost all $\mathcal{S}(Z, z)$; a knee at $M_{\rm BH,1} \approx 35 M_{\odot}$ and another bump at $M_{\rm BH,1} \approx 45 M_{\odot}$. Although the locations of these features are constant, the features themselves can disappear for variations that suppress the rate of high mass BHs (e.g., dashed lines in the top panels of Figure 3). Similarly, the CE channel displays a kink in the distribution at about $9 M_{\odot}$, and a peak at approximately $M_{\rm BH,1} \approx 17 M_{\odot}$ for all variations. The latter peak is the global peak of the mass distribution in almost all variations.

The finding that the locations of features in the mass distribution do not change for different $\mathcal{S}(Z, z)$ is consistent with earlier work. Recent work by Chruślińska (2022) showed that, when comparing two very different models of $\mathcal{S}(Z, z)$ (their Figure 5), the location of the peaks remains the same, even though the normalization between the two BBH merger rates is completely different. Furthermore, Broekgaarden et al. (2022) show the probability distribution of chirp masses for BBHs in their Figure 4. Although features can disappear when the $\mathcal{S}(Z, z)$ prohibits the formation of certain (typically higher) mass BHs, the *location* of features remains the same. This implies that the locations of features in the mass distribution of BBHs are determined by the formation channel and its underlying stellar and binary physics. The locations of features could therefore serve as signposts of the underlying physics.

Second, we see that the low-mass end of the primary mass distribution is relatively robust against variations in $\mathcal{S}(Z, z)$. To quantify this, we annotate the ratio between the maximum and minimum rate at three reference masses; $M_{\rm BH,1} = 10$, 25, and $40 M_{\odot}$. At $M_{\rm BH,1} = 10 M_{\odot}$, we find that the rate changes by at most a factor of about 3.7 for the stable channel, and at most about a factor of 3.8 for the CE channel. On the other hand, the change in rate at $M_{\rm BH,1} = 40 M_{\odot}$ can be as high as a factor of about 200 and 150 for the stable and CE channels, respectively. The lowest mass BHs are least affected by the $\mathcal{S}(Z, z)$ because they can be formed from all metallicities above $Z \gtrsim 10^{-3}$ (see, e.g., Figures 7 and 13 in van Son et al. 2022a). The SFR at metallicities above $\gtrsim 10^{-3}$ is observationally relatively well constrained for redshifts below 0.5 (which comprises the past 5 Gyr of star formation). This is reflected in the top panel of Figure 6 all models show that 10% or less of the stellar mass was formed at a metallicity below $Z/10 \approx 0.0014$, or in other words, about 90% or more of the stellar mass was formed at a metallicity above $Z/10$. Hence, the lowest mass BHs derive from the least uncertain parts of the $\mathcal{S}(Z, z)$. The low-mass end of the mass distribution of merging double compact objects will also provide a particularly powerful cosmological constraint in the era of third-generation GW telescopes (María Ezquiaga & Holz 2022). Our finding that the low-mass end is more robust against variations in $\mathcal{S}(Z, z)$ supports this claim.

Parameter variations that affect shape of $\mathcal{S}(Z, z)$ at low redshift primarily change the normalization of the mass distribution. This is the case for variations of the width of the cosmic metallicity density distribution at $z = 0$ (ω_0), the mean metallicity of the cosmic metallicity density distribution at $z = 0$ (μ_0), and the skewness of the cosmic metallicity density distribution (α, left columns of Figures 3 and 4). To emphasize this point, we annotate the total BBH merger rate at redshift 0.2, $\mathcal{R}_{0.2}$, in the legends of Figures 3 and 4 (0.2 is the redshift where the observations are best constrained Abbott et al. 2021c). Variations that increase the amount of star formation at low metallicity (i.e., for a low mean metallicity $\mu_0 = 0.007$ and a wide metallicity distribution $\omega_0 = 2.0$) increase the predicted BBH merger rate. This is consistent with other work that finds merging BBHs form more efficiently at low metallicities (e.g., Belczynski et al. 2010; Mapelli et al. 2017; Stevenson et al. 2017; Chruślińska et al. 2019; Broekgaarden et al. 2022). A

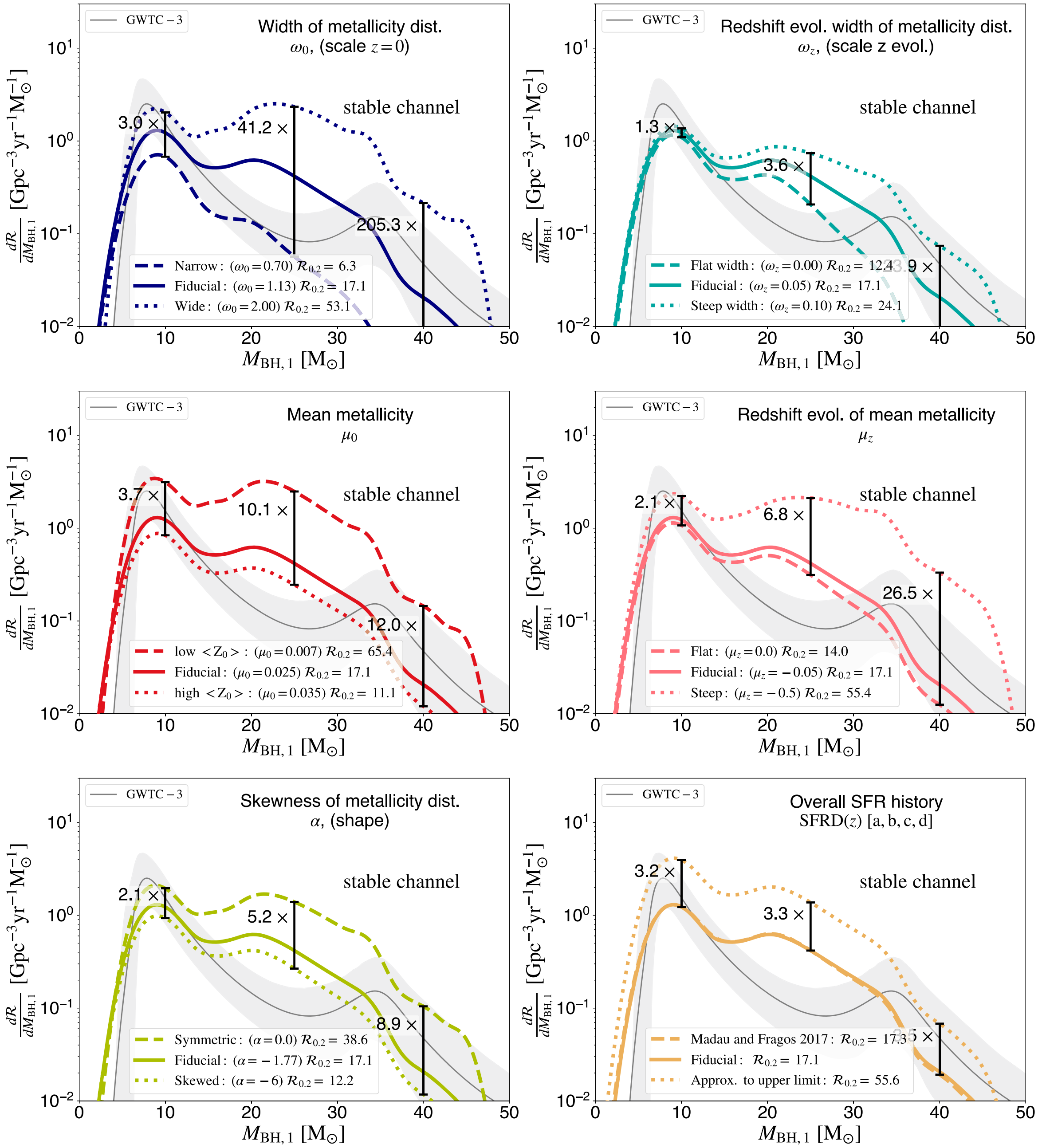

Figure 3. The primary mass distribution of merging BBH systems from the stable mass transfer channel for several variations in $\mathcal{S}(Z, z)$. The first five panels show variations of the cosmic metallicity density distribution $dP/dZ(Z, z)$, Equation (11), (parameters listed in the first three columns of Table 1), where we vary one parameter at a time while keeping the rest fixed at their fiducial value. The bottom right panel shows variations in the magnitude of the SFR with redshift, i.e., SFRD (z). For the latter, we vary the four fiducial parameters of SFRD(z) simultaneously (last two columns of Table 1). All panels are shown at a reference redshift of $z = 0.2$, with the corresponding predicted BBH merger rate indicated in the legend. For reference, we show the power-law + peak model from Abbott et al. (2021c) in gray. We annotate the relative change in the rate at three reference masses: 10, 25, and $40 M_\odot$.

more skewed cosmic metallicity density distribution pushes the peak of the distribution to higher metallicities and thus forms more stars at high metallicity when compared to a symmetric distribution. Hence, the local rate of BBH mergers is lower for the skewed distribution ($\alpha = -6$) with respect to the symmetric variation ($\alpha = 0.0$).

Changing the overall SFRD(z) (bottom right panels of Figures 3 and 4) also affects the normalization of the mass distribution, but has a smaller effect than the width and the mean of the cosmic metallicity density distribution at $z = 0$ (ω_0 and μ_0). This underlines the importance of the amount of low-metallicity star formation (e.g., Chruślińska 2022), and is furthermore in line with findings from Tang et al. (2020). As discussed in Section 4.1, we use Madau & Fragos (2017) and the solid blue line in Figure 2 as an approximate lower and upper bound to the SFRD(z), respectively. The overall cosmic SFR from Madau & Fragos (2017) is very similar to our fiducial model (Figure 2), and the differences between the resulting mass distributions are correspondingly small. Our approximation of the upper limit to the allowed SFRD(z) leads to an overall increase of the BBH merger rate by a factor of about 3.

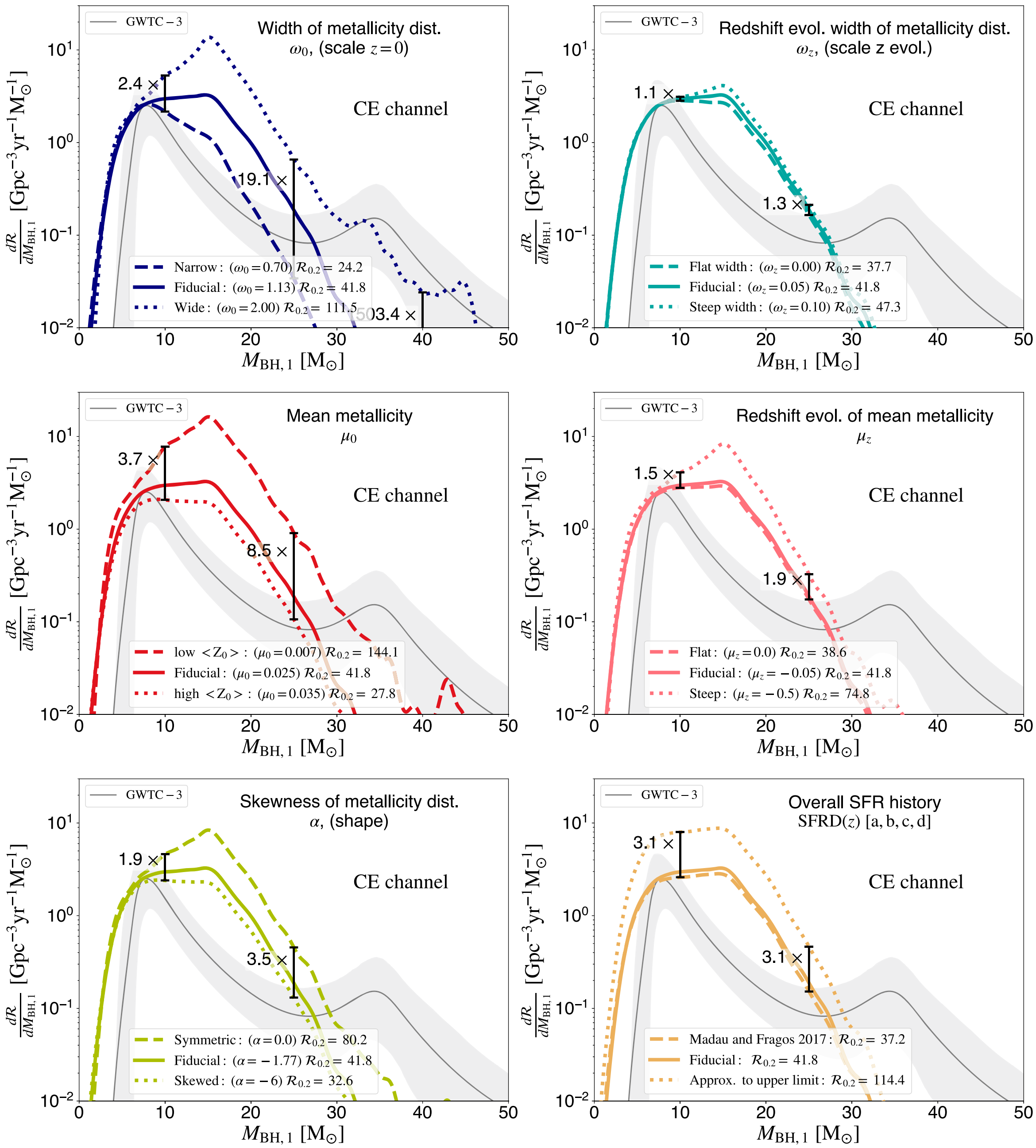

Figure 4. Same as Figure 3, but for the CE channel. These figures show that the low-mass end of the primary mass distribution is least affected by the adopted $\mathcal{S}(Z, z)$. Moreover, the *locations* of features in the mass distribution are robust against all explored variations.

Parameters that change the evolution of the metallicity distribution $dP/dZ(Z, z)$ with redshift, such as the redshift dependence of the with and mean; ω_z and μ_z (top right and center-right panels of Figures 3 and 4) primarily affect the high mass end of the stable channel. We understand this as an effect of the different delay time distributions for both formation channels. Since both, ω_z and μ_z influence the amount of low-metallicity stellar mass formed at high redshifts they will mostly affect systems with longer delay times. The stable channel has been shown to produce more high-mass BHs with longer delay times when compared to the CE channel (Briel et al. 2023; van Son et al. 2022a). Hence, we find these variations affect the slope of the high mass end of the BBH mass distribution for the stable channel, while they have a relatively small impact on the CE channel.

5. Discussion and Summary

We present a flexible analytic expression for the metallicity-dependent cosmic star formation history, $\mathcal{S}(Z, z)$ (Equations (1), (11), and (12)). An analytical expression allows for controlled experiments of the effect of $\mathcal{S}(Z, z)$ on dependent values, such as the rate and mass distribution of merging BBHs. The model presented in this work adopts a skewed-log normal for the distribution of metallicities at every redshift ($dP/dZ(Z, z)$).

The model can capture the general behavior of cosmological simulations, such as TNG100—Our analytical expression for $\mathcal{S}(Z, z)$ is composed of a cosmic metallicity density distribution that is determined by a mean, scale, and skewness and their redshift dependence, as well as parameters governing the overall SFR. We fit our analytical expression for $\mathcal{S}(Z, z)$ to the star-forming gas in the TNG100 simulation, and provide the best-fit parameters in Table 1. We show that our model captures the shape and general behavior of the cosmological simulations well (Figure 1). Although our model is more broadly applicable than previous models, we acknowledge that it does not capture the *complete* range of observationally allowed variations in it is current form. Incorporating more complex functions for the redshift evolution of the metallicity could solve this issue, but this is left for future research.

The model allows for a controlled experiment on the effect of $\mathcal{S}(Z, z)$ on the local distribution of merging BBH—As an example, we use our model to calculate the local rate and mass distribution of the more massive components from merging BBHs ($M_{\rm BH,1}$) in Figures 3 and 4. We systematically vary all five parameters that shape the cosmic metallicity density distribution, and explore two additional variations of the overall SFRD(z). Our main findings are as follows:

1. The locations of features in the distribution of primary BH masses are robust against variations in $\mathcal{S}(Z, z)$. The location of features in the mass distribution of BHs could thus be used as sign posts of their formation channel.
2. For all variations, the low-mass end of the mass distribution is least influenced by changes in the $\mathcal{S}(Z, z)$. This is because the lowest mass BHs can be formed from all metallicities above $Z \gtrsim 10^{-3}$, for which the SFR is relatively well constrained in the recent universe. This suggests that the lower end of the BH mass distribution (component masses of $\leqslant 15 M_{\odot}$) is potentially very powerful for constraining the physics of the formation channels, irrespective of the cosmic star formation rate uncertainties.
3. The metallicity distribution of star formation at low redshift primarily impacts the normalization of the BBH merger rate. Changing the overall star formation rate density, SFRD(z) also affects the rate, but to a lesser degree. This shows that low-metallicity star formation at low redshifts dominates the overall normalization of the BBH merger rate.
4. Parameters that influence the redshift evolution of the mean and the width of the metallicity distribution affect the slope of the high mass end of the primary BH mass distribution for the stable channel. This reflects the longer delay times of the stable channel with respect to the CE channel.

The flexibility of the model presented in this work can capture the large uncertainties that remain in the shape and normalization of the metallicity-dependent cosmic star formation history. Our hope is that this expression will provide a useful starting point for making predictions and comparisons with observations.

The authors acknowledge partial financial support from the National Science Foundation under grant No. (NSF grant No. 2009131 and PHY-1748958)", the Netherlands Organization for Scientific Research (NWO) as part of the Vidi research program BinWaves with project number 639.042.728 and the European Union's Horizon 2020 research and innovation program from the European Research Council (ERC, grant agreement No. 715063). This research was supported in part by the National Science Foundation under grant No. NSF PHY-1748958.

Software and Data

All code associated to reproduce the data and plots in this paper is publicly available at https://github.com/LiekeVanSon/SFRD_fit. The data used in this work is available on Zenodo under an open-source Creative Commons Attribution license at doi:10.5281/zenodo.7612755. All observationally constrained models of the $\mathcal{S}(Z, z)$ from Chruślińska et al. (2021) can be found online at https://ftp.science.ru.nl/astro/mchruslinska/Chruslinska_et_al_2021/.

This research has made use of GW data provided by the Gravitational Wave Open Science Center (https://www.gw-openscience.org/), a service of LIGO Laboratory, the LIGO Scientific Collaboration, and the Virgo Collaboration. Further software used in this work: Python (Van Rossum & Drake 2009), Astropy (Astropy Collaboration et al. 2013, 2018) Matplotlib (Hunter 2007), NumPy (Harris et al. 2020), SciPy (Virtanen et al. 2020), `ipython/jupyter` (Perez & Granger 2007; Kluyver et al. 2016), Seaborn (Waskom 2021) and hdf5 (Collette et al. 2019).

Appendix A
Evaluating Our Fit: The Squared Residuals

In the left panel of Figure 5, we show the log of the absolute residuals. The *square* of the residuals is used in the cost function, Equation (14), to optimize our fit. We observe that the maximum residuals appear near the peak of star formation at high metallicities. The log of the relative errors (defined as $\frac{|\mathcal{S}{\rm sim} - \mathcal{S}{\rm fit}|}{\mathcal{S}_{\rm fit}}$), is shown in the right-hand panel of Figure 5. The relative errors generally exhibit an opposite trend with respect to the residuals. The relative errors are largest in regions of very low-metallicity star formation at low redshift. This occurs due to the very low star formation rate in this regime (of the order $10^{-8} M_{\odot}\,{\rm yr}^{-1}\,{\rm Mpc}^{-3}$ for the TNG simulations and $10^{-11} M_{\odot}\,{\rm yr}^{-1}\,{\rm Mpc}^{-3}$ in our model fit). Another regime where the relative error becomes large is at very high metallicities (about 10 times $Z_{\odot}$). This is because in this regime, the TNG data is very sparse and contains regions where the rate abruptly drops to zero. To avoid sharp features in the data, we use interpolated TNG data to produce the fit. We note that we chose to minimize the squared residuals (which is similar to minimizing the mean squared error) in favor of minimizing, for example, the relative error, to prevent overfitting such regions of very low star formation rate. For illustration purposes in this work, we are most interested in closely fitting the $\mathcal{S}(Z, z)$ between the minimum (10^{-4}) and maximum (0.03) metallicities that can be simulated with `COMPAS`. For applications that focus on extremely low ($<0.01 Z_{\odot}$) or extremely high ($\sim 10 \times Z_{\odot}$) metallicity star formation, a different cost function would be more appropriate.

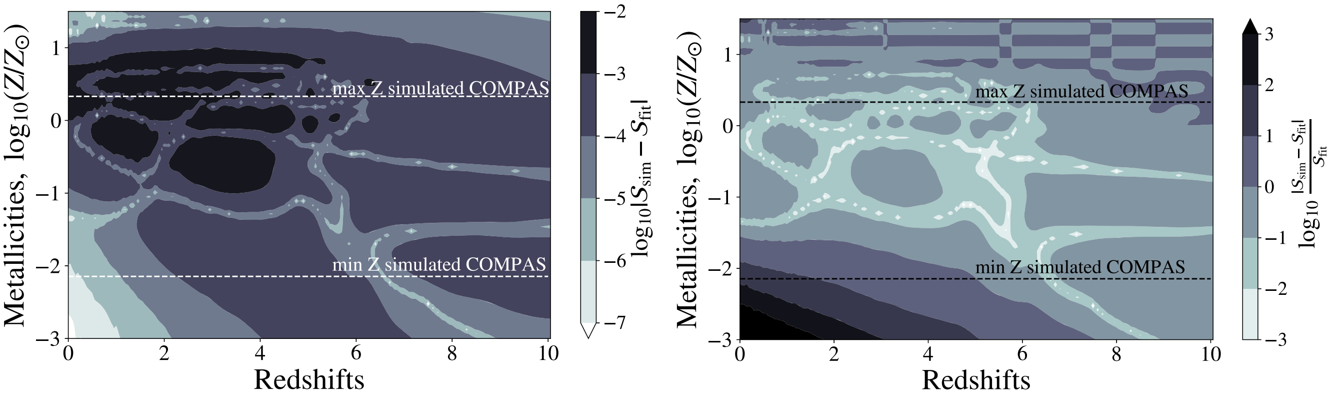

Figure 5. log of the residuals (left), and log of the relative error (right) between the TNG100 data and our best-fitting model. We show the minimum and maximum metallicity used in `COMPAS` simulations with dashed lines in each plot.

Appendix B
Determining Reasonable Variations of the $\mathcal{S}(Z, z)$

To determine reasonable variations of our fiducial model for $\mathcal{S}(Z, z)$, we compute the fraction of low and high metallicity stellar mass formed for redshifts below $z < 0.5$, 3.0, and 10. We show the results in Figure 6, which is an adaptation of Figure 2 in Pakmor et al. (2022), which in turn builds on Figure 9 from Chruślińska & Nelemans (2019).

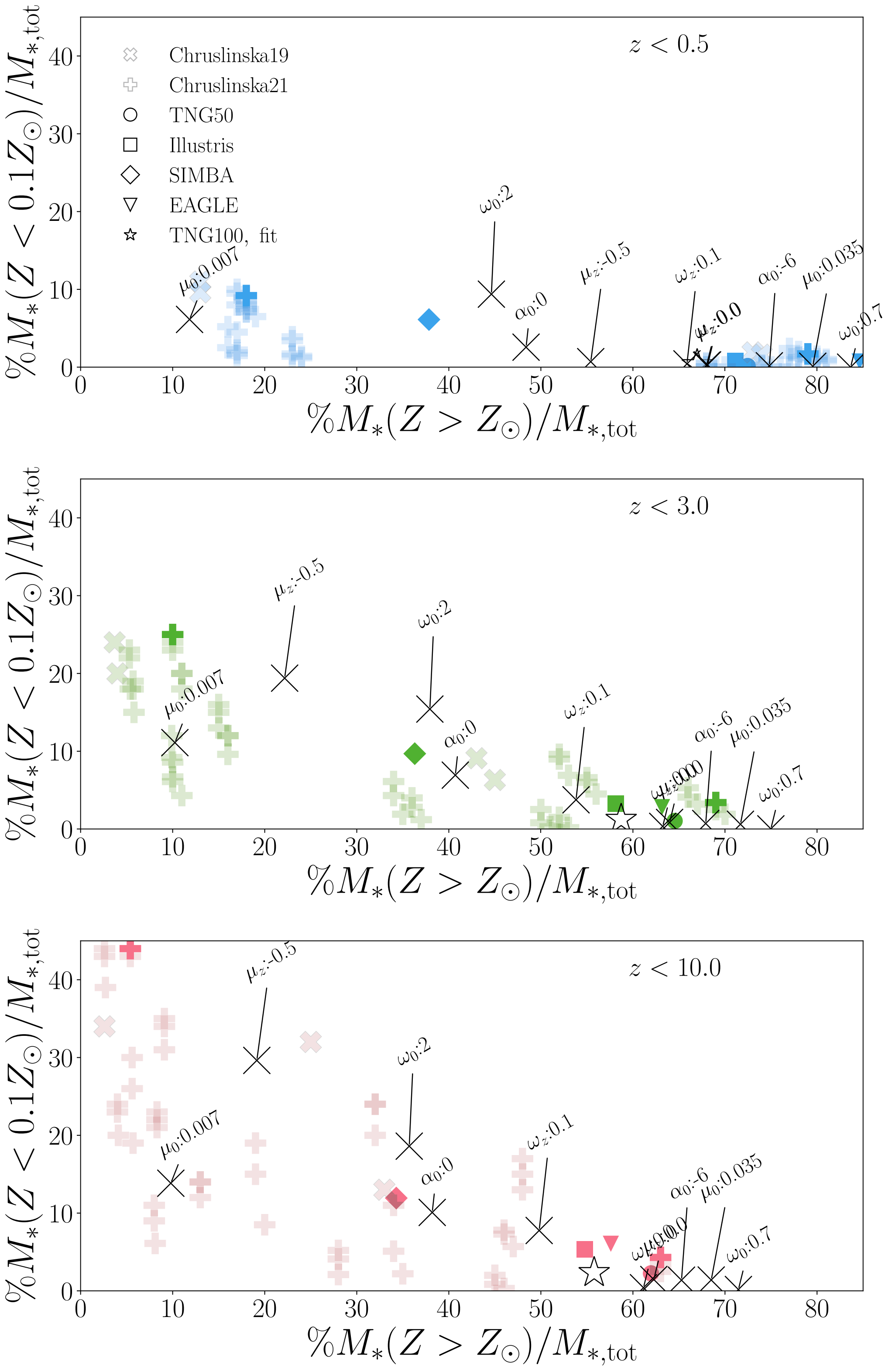

Figure 6. Percentage of stellar mass formed at low metallicity ($Z < 0.1Z_\odot$), vs. high metallicity ($Z > Z_\odot$) for all star formation below a certain threshold redshift: $z < 0.5$ (top), $z < 3.0$ (middle) and $z < 10$ (bottom). Data from observation-based variations are shown with semitransparent thick crosses, Chruślińska & Nelemans (2019) and semitransparent thick plus signs (Chruślińska et al. 2021), the low- and high-metallicity extremes are indicated with opaque symbols. For data from cosmological simulations, we follow Pakmor et al. (2022) and show Illustris (Vogelsberger et al. 2014, squares), Simba (Davé et al. 2019, diamonds), EAGLE (Schaye et al. 2015, triangles), TNG50 and TNG100 (Springel et al. 2018, filled and open circles, respectively). Black thin crosses display variations of the cosmic metallicity density distribution that is part of our fiducial $\mathcal{S}(Z, z)$. The parameter that is varied with respect to the fiducial and its new value are annotated. This shows that our $\mathcal{S}(Z, z)$ variations span the range of reasonable cosmic metallicity density distributions as determined by observation-based and cosmological simulation-based models.

ORCID iDs

L. A. C. van Son https://orcid.org/0000-0001-5484-4987
S. E. de Mink https://orcid.org/0000-0001-9336-2825
M. Chruślińska https://orcid.org/0000-0002-8901-6994
C. Conroy https://orcid.org/0000-0002-1590-8551
R. Pakmor https://orcid.org/0000-0003-3308-2420
L. Hernquist https://orcid.org/0000-0001-6950-1629

References

Abbott, B. P., Abbott, R., Abbott, T. D., et al. 2016, ApJL, 818, L22
Abbott, B. P., Abbott, R., Abbott, T. D., et al. 2019, PhRvX, 9, 031040
Abbott, R., Abbott, T. D., Abraham, S., et al. 2021a, PhRvX, 11, 021053
Abbott, R., Abbott, T. D., Acernese, F., et al. 2021b, arXiv:2111.03606
Abbott, R., Abbott, T. D., Acernese, F., et al. 2021c, arXiv:2111.03634
Astropy Collaboration, Price-Whelan, A. M., Sipőcz, B. M., et al. 2018, AJ, 156, 123
Astropy Collaboration, Robitaille, T. P., Tollerud, E. J., et al. 2013, A&A, 558, A33
Bavera, S. S., Fragos, T., Zapartas, E., et al. 2022, A&A, 657, L8
Bavera, S. S., Fragos, T., Zevin, M., et al. 2021, A&A, 647, A153
Belczynski, K., Bulik, T., Fryer, C. L., et al. 2010, ApJ, 714, 1217
Belczynski, K., Holz, D. E., Bulik, T., & O'Shaughnessy, R. 2016, Natur, 534, 512
Belczynski, K., Taam, R. E., Kalogera, V., Rasio, F. A., & Bulik, T. 2007, ApJ, 662, 504
Bisigello, L., Caputi, K. I., Grogin, N., & Koekemoer, A. 2018, A&A, 609, A82
Boco, L., Lapi, A., Chruslinska, M., et al. 2021, ApJ, 907, 110
Briel, M. M., Eldridge, J. J., Stanway, E. R., Stevance, H. F., & Chrimes, A. A. 2022, MNRAS, 514, 1315
Briel, M. M., Stevance, H. F., & Eldridge, J. J. 2023, MNRAS, 520, 5724
Broekgaarden, F. S., Berger, E., Stevenson, S., et al. 2022, MNRAS, 516, 5737
Caputi, K. I., Deshmukh, S., Ashby, M. L. N., et al. 2017, ApJ, 849, 45
Chruślińska, M. 2022, arXiv:2206.10622
Chruślińska, M., & Nelemans, G. 2019, MNRAS, 488, 5300
Chruślińska, M., Nelemans, G., & Belczynski, K. 2019, MNRAS, 482, 5012
Chruślińska, M., Nelemans, G., Boco, L., & Lapi, A. 2021, MNRAS, 508, 4994
Collette, A., Caswell, T. A., Tocknell, J., et al. 2019, h5py/h5py: v2.10.0, Zenodo, doi:10.5281/zenodo.3401726
Cresci, G., Mannucci, F., & Curti, M. 2019, A&A, 627, A42
Davé, R., Anglés-Alcázar, D., Narayanan, D., et al. 2019, MNRAS, 486, 2827
Dominik, M., Belczynski, K., Fryer, C., et al. 2013, ApJ, 779, 72
Dominik, M., Berti, E., O'Shaughnessy, R., et al. 2015, ApJ, 806, 263
Doughty, C., & Finlator, K. 2021, MNRAS, 505, 2207
Dray, L. M., Tout, C. A., Karakas, A. I., & Lattanzio, J. C. 2003, MNRAS, 338, 973
Farmer, R., Laplace, E., de Mink, S. E., & Justham, S. 2021, ApJ, 923, 214
Fruchter, A. S., Levan, A. J., Strolger, L., et al. 2006, Natur, 441, 463
Gallegos-Garcia, M., Berry, C. P. L., Marchant, P., & Kalogera, V. 2021, ApJ, 922, 110
Goswami, S., Silva, L., Bressan, A., et al. 2022, A&A, 663, A1
Götberg, Y., de Mink, S. E., McQuinn, M., et al. 2020, A&A, 634, A134
Harris, C. R., Millman, K. J., van der Walt, S. J., et al. 2020, Natur, 585, 357
Hemler, Z. S., Torrey, P., Qi, J., et al. 2021, MNRAS, 506, 3024
Hunter, J. D. 2007, CSE, 9, 90
Hurley, J. R., Pols, O. R., & Tout, C. A. 2000, MNRAS, 315, 543
Hurley, J. R., Tout, C. A., & Pols, O. R. 2002, MNRAS, 329, 897
Inayoshi, K., Hirai, R., Kinugawa, T., & Hotokezaka, K. 2017, MNRAS, 468, 5020
Kennicutt, R. C., Jr. 1989, ApJ, 344, 685
Kewley, L. J., & Ellison, S. L. 2008, ApJ, 681, 1183
Kluyver, T., Ragan-Kelley, B., Pérez, F., et al. 2016, in Positioning and Power in Academic Publishing: Players, Agents and Agendas, ed. F. Loizides & B. Schmidt (Amsterdam: IOS Press), 87
Kobulnicky, H. A., & Kewley, L. J. 2004, ApJ, 617, 240
Kroupa, P. 2001, MNRAS, 322, 231
Kummer, F. 2020, Master's Thesis, Univ. of Amsterdam https://scripties.uba.uva.nl/
Langer, N., & Norman, C. A. 2006, ApJL, 638, L63
Langer, N., Norman, C. A., de Koter, A., et al. 2007, A&A, 475, L19
Madau, P., & Dickinson, M. 2014, ARA&A, 52, 415
Madau, P., & Fragos, T. 2017, ApJ, 840, 39
Maiolino, R., & Mannucci, F. 2019, A&ARv, 27, 3
Mapelli, M., Giacobbo, N., Ripamonti, E., & Spera, M. 2017, MNRAS, 472, 2422
Marchant, P., Pappas, K. M. W., Gallegos-Garcia, M., et al. 2021, A&A, 650, 107
María Ezquiaga, J., & Holz, D. E. 2022, PhRvL, 129, 061102
Marinacci, F., Vogelsberger, M., Pakmor, R., et al. 2018, MNRAS, 480, 5113
Naiman, J. P., Pillepich, A., Springel, V., et al. 2018, MNRAS, 477, 1206
Neijssel, C. J., Vigna-Gómez, A., Stevenson, S., et al. 2019, MNRAS, 490, 3740
Nelson, D., Pillepich, A., Springel, V., et al. 2018, MNRAS, 475, 624
Nelson, D., Pillepich, A., Springel, V., et al. 2019a, MNRAS, 490, 3234
Nelson, D., Springel, V., Pillepich, A., et al. 2019b, ComAC, 6, 2
Nelson, E. J., Tacchella, S., Diemer, B., et al. 2021, MNRAS, 508, 219
Nocedal, J., & Wright, S. 2006, Numerical Optimization (2nd ed.; New York: Springer)
O'Hagan, A., & Leonard, T. O. M. 1976, Biometrika, 63, 201
Pakmor, R., Simpson, C. M., van de Voort, F., et al. 2022, MNRAS, 512, 3602
Perez, F., & Granger, B. E. 2007, CSE, 9, 21
Pettini, M., & Pagel, B. E. J. 2004, MNRAS, 348, L59
Pillepich, A., Nelson, D., Hernquist, L., et al. 2018a, MNRAS, 475, 648
Pillepich, A., Nelson, D., Springel, V., et al. 2019, MNRAS, 490, 3196
Pillepich, A., Springel, V., Nelson, D., et al. 2018b, MNRAS, 473, 4077
Planck Collaboration, Aghanim, N., Akrami, Y., et al. 2020, A&A, 641, A6
Pols, O. R., Schröder, K.-P., Hurley, J. R., Tout, C. A., & Eggleton, P. P. 1998, MNRAS, 298, 525
Postnov, K. A., & Yungelson, L. R. 2014, LRR, 17, 3
Riley, J., Agrawal, P., Barrett, J. W., et al. 2022, ApJS, 258, 34
Sanders, R. L., Shapley, A. E., Clarke, L., et al. 2023, ApJ, 943, 75
Santoliquido, F., Mapelli, M., Giacobbo, N., Bouffanais, Y., & Artale, M. C. 2021, MNRAS, 502, 4877
Schaye, J., Crain, R. A., Bower, R. G., et al. 2015, MNRAS, 446, 521
Schmidt, M. 1959, ApJ, 129, 243
Smith, N. 2014, ARA&A, 52, 487
Springel, V., Di Matteo, T., & Hernquist, L. 2005, MNRAS, 361, 776
Springel, V., & Hernquist, L. 2003, MNRAS, 339, 289
Springel, V., Pakmor, R., Pillepich, A., et al. 2018, MNRAS, 475, 676
Stevenson, S., Vigna-Gómez, A., Mandel, I., et al. 2017, NatCo, 8, 14906
Tang, P. N., Eldridge, J. J., Stanway, E. R., & Bray, J. C. 2020, MNRAS, 493, L6
Torrey, P., Vogelsberger, M., Marinacci, F., et al. 2019, MNRAS, 484, 5587
van den Heuvel, E. P. J., Portegies Zwart, S. F., & de Mink, S. E. 2017, MNRAS, 471, 4256
Van Rossum, G., & Drake, F. L. 2009, Python 3 Reference Manual (Scotts Valley, CA: CreateSpace)
van Son, L. A. C., de Mink, S. E., Callister, T., et al. 2022a, ApJ, 931, 17
van Son, L. A. C., de Mink, S. E., Renzo, M., et al. 2022b, ApJ, 940, 184
Vigna-Gómez, A., Neijssel, C. J., Stevenson, S., et al. 2018, MNRAS, 481, 4009
Virtanen, P., Gommers, R., Oliphant, T. E., et al. 2020, NatMe, 17, 261
Vogelsberger, M., Genel, S., Springel, V., et al. 2014, MNRAS, 444, 1518
Wang, K., Yu, S., & Peng, W. 2019, JAerS, 134, 95
Waskom, M. 2021, JOSS, 6, 3021
Weinberger, R., Springel, V., Hernquist, L., et al. 2017, MNRAS, 465, 3291